1   **Title: Improved mammalian retromer cryo-EM structures reveal a new assembly interface**

2

3   **Running title: Retromer cryo-EM reveals new interface**

4

5   Amy K. Kendall[1,2], Mintu Chandra[1,2], Boyang Xie[1], William Wan[2,3], and Lauren P. Jackson[1,2,3]

6

7   [1]Department of Biological Sciences, Vanderbilt University, Nashville, TN, USA

8   [2]Center for Structural Biology, Vanderbilt University, Nashville, TN, USA

9   [3]Department of Biochemistry, Vanderbilt University, Nashville, TN, USA

10

11   [†]Correspondence to lauren.p.jackson@vanderbilt.edu

12

13   **Abstract**

14   Retromer (VPS26/VPS35/VPS29 subunits) assembles with multiple sorting nexin (SNX)

15   proteins on membranes to mediate endosomal recycling of transmembrane protein cargoes.

16   Retromer has been implicated in other cellular events, including mitochondrial homeostasis,

17   nutrient sensing, autophagy, and fission events. Mechanisms for mammalian retromer assembly

18   remain undefined, and retromer engages multiple sorting nexin proteins to sort cargoes to

19   different destinations. Published structures demonstrate mammalian retromer forms oligomers *in*

20   *vitro*, but several structures were poorly resolved. We report here improved retromer oligomer

21   structures using single particle cryo-electron microscopy (cryo-EM) by combining data collected

22   from tilted specimens with multiple improvements in data processing, including using a three-

23   dimensional (3D) starting model for improved automated particle picking in RELION. A

24   retromer mutant (3KE retromer) that breaks VPS35-mediated interfaces was used to determine a

25   structure of a new assembly interface formed by the VPS26A and VPS35 N-termini. The

26   interface reveals how an N-terminal VPS26A arrestin saddle can link retromer chains by

27   engaging a neighboring VPS35 N-terminus, on the opposite side from the well-characterized C-

28   VPS26/N-VPS35 interaction observed within heterotrimers. The new interaction interface

29   exhibits substantial buried surface area (~7,000 Å^2) and further suggests metazoan retromer may

30   serve as an adaptable scaffold.

31

1

32   **Introduction**

33   Eukaryotic cells contain multiple membrane-enclosed organelles, which dynamically

34   communicate with each other through membrane trafficking pathways. Trafficking ensures

35   exchange of lipid and protein cargoes between donor and acceptor compartments, and trafficking

36   events are spatiotemporally regulated by multiple large multi-protein complexes. Retromer

37   (VPS26/VPS35/VPS29 subunits) is one important complex that plays a well-established role in

38   protein sorting at endosomes by maintaining dynamic localization of hundreds of transmembrane

39   proteins that traverse the endocytic system. Mammalian retromer associates with the cytosolic

40   face of endosomes, where it functions to recycle receptors, transporters, and adhesion molecules.

41   Retromer is thought to mediate retrograde recycling to the *trans*-Golgi network (TGN) (*1–3*) or

42   to the plasma membrane (*4–7*) through sorting into tubular-vesicular carriers (reviewed in (*8–*

43   *10*)). Retromer-dependent cargoes undergo selective trafficking to avoid sorting to late

44   endosomes and subsequent degradation in lysosomes (*11*), which ensures cells maintain

45   homeostasis of transmembrane cargoes at the plasma membrane and within the endolysosomal

46   system. Retromer trafficking pathways become dysregulated in multiple ways, including aberrant

47   protein processing (*12*) and sorting (*13, 14*). Disruptions to retromer trafficking in turn drive

48   protein misfolding linked with neurological and neurodegenerative conditions, including

49   Alzheimer's disease (AD) (*15–17*), Parkinson's disease (PD) (*18*), and Down's syndrome (*19,*

50   *20*). Retromer pathways can also be hijacked by both bacterial and viral pathogens (*21, 22*).

51

52   Retromer is thus well established as an evolutionarily conserved heterotrimer that binds different

53   Sorting Nexin (SNX) proteins to mediate cargo sorting from phosphatidylinositol-3-phosphate

54   (PtdIns3*P*)-enriched endosomal membranes. Retromer binds multiple sorting nexin family

55   members, including SNX-BARs, SNX3, and metazoan-specific SNX27 (reviewed recently in

56   (*10, 23, 24*)). The retromer heterotrimer (formerly called Cargo Selective Complex, or CSC) has

57   been implicated in direct cargo recognition in both mammalian cells (*2, 25*) and yeast (*1, 26*).

58   More recently, SNX-BARs have been shown to bind cargo directly in mammalian cells (*27, 28*),

59   and SNX3 promotes cargo recognition in both yeast (*29, 30*) and mammalian cells (*31*). Yeast

60   SNX-BAR/retromer (*32*) and both yeast and mammalian SNX3/retromer (*33*) complexes have

61   been shown to form tubules *in vitro*. SNXs may therefore be considered critical adaptors that

2

62   promote membrane recruitment (*5*, *34*); recognize cargo (*6*, *27*, *31*, *35*, *36*); and drive tubule

63   formation (*34*).

64

65   From a structural viewpoint, multiple crystal (*31*, *37–39*), single particle cryo-EM (*40*), and

66   cryo-ET (*32*, *33*) structures have revealed how retromer subunits fold in three-dimensional

67   space; how subunits interact to form a stable and elongated heterotrimer; and how heterotrimers

68   assemble *in vitro* to form higher order oligomers in vitreous ice (*40*) or assembled on membranes

69   with sorting nexins (*32*, *33*). Briefly, VPS35 adopts an elongated α-helical solenoid fold. VPS26

70   exists as three orthologues in mammals (VPS26A/VPS26B/VPS26C) and adopts a bi-lobal

71   arrestin-like fold (*39*, *41*). VPS26A and VPS26B bind the highly conserved VPS35 N-terminus

72   (*39*), while VPS26C binds VPS35-like (VPS35L) in the retriever complex (*42*). VPS29 contains

73   a metallophosphoesterase fold (*38*, *43*) that serves as a scaffold for binding the α-helical solenoid

74   of the VPS35 C-terminus (*31*, *37*, *40*). Cryo-ET reconstructions revealed how retromer

75   assembles with either SNX-BAR or SNX3 on membranes. Retromer assembles on top of either

76   SNX-BAR dimers or SNX3 to form high V-shaped arches mediated by interactions between

77   VPS35 subunits. Back-to-back VPS26 dimers mediate interactions with SNX-BARs or SNX3. In

78   solution, mammalian retromer forms multiple oligomers, including the retromer heterotrimer;

79   dimers of trimers; a tetramer of trimers; and extended flat chains (*40*). The existence of multiple

80   oligomeric assemblies suggests mammalian retromer may function as a flexible scaffold. Single

81   particle and biochemical data revealed critical residues in the VPS35/VPS35 assembly interface,

82   which was tested biochemically and in yeast (*40*) and subsequently reported in cryo-ET

83   reconstructions (*33*). The cryo-ET and single particle reconstructions share several common

84   themes. The mammalian VPS35/VPS35 dimer interface resembles yeast VPS35 dimers observed

85   at the top of the V-shaped arches (*32*, *33*). However, the curvature of the mammalian VPS35

86   interfaces observed in dimers and chains differs, which results in long and flat chains (*40*).

87   Additionally, mammalian retromer appears to form a VPS26A-mediated "tip to tip" dimer (*40*)

88   that differs from back-to-back VPS26 dimers observed in the presence of SNX3 (*33*) or the yeast

89   SNX-BAR,Vps5 (*32*). The mammalian VPS26 "chain link" interface was poorly resolved

90   because particles exhibit severely preferred orientation. These data suggest VPS26 may be

91   capable of forming at least two different dimers, but the biological context of the "tip-to-tip"

92 dimers remains unknown. Improved structural data for this putative interface is important so that

93 structural models can be used to test function in cell culture or model organisms.

94

95 In this work, we report improved single particle cryo-EM reconstructions of multiple mammalian

96 retromer oligomers, including the heterotrimer, dimers of trimers, and two VPS35/VPS35 sub-

97 structures. These improved structural models arise from multiple improvements implemented

98 during data collection and processing. Acquisition of tilted datasets provided critical missing

99 views for some particles. For some structures, early rounds of automated particle picking using a

100 three-dimensional (3D) starting model in RELION also provided additional views. Map

101 sharpening followed by real space refinement in PHENIX resulted in improved heterotrimer

102 reconstructions that allowed subunits to be assigned in maps more confidently. We further report

103 a new structure of the N-VPS26A/N-VPS35 "chain link" interface using a retromer mutant (3KE

104 mutant) that breaks VPS35 interfaces in chains (*40*). This new interface is formed by interactions

105 between the VPS26A N-terminal arrestin fold with the N-terminus of VPS35 in a neighboring

106 heterotrimer. The presence of this particle *in vitro* suggests retromer may be capable of forming a

107 variety of assemblies, even in the absence of sorting nexin proteins.

108

109 **Results**

110

111 *Retromer heterotrimer.* To generate improved reconstructions, we combined images from

112 previously published data (*40*) with a new third data set in which specimens were tilted to gain

113 additional views (Figure S1; Table 1) (*44*). We obtained an improved heterotrimer reconstruction

114 from 43,808 particles with an average resolution of 4.9 Å. Figure 1 formally compares this

115 structure (panels A, C, E, G; (*44*)) with the previously published version (panels B, D, F, H;

116 (*40*)). Critical missing views were acquired from the additional tilted data set (Figure 1E versus

117 1F). Map sharpening in PHENIX followed by several rounds of refinement and model building

118 (see Methods) substantially improved the heterotrimer model (Figure 1A; 1G; Table 2). This

119 structure demonstrates improved local resolution across the heterotrimer (Figure 1C, 1D). In the

120 previous version (*40*), the N-VPS35/C-VPS26 interface was poorly resolved (Figure 1B, 1D)

121 compared to the VPS35/VPS29 interface. In the new structure, the arrestin "saddle" fold of

4

122   VPS26 is more clearly resolved (Figure 1A, 1G). Overall, improvements in both data collection

123   and processing (see Discussion) played a key role in generating a higher quality reconstruction.

124

125   *Retromer dimers of trimers*. Retromer has been shown to form "dimers of heterotrimers" using

126   both biophysical (*40, 45*) and structural (*40*) methods. In all reported conditions, formation of

127   retromer dimers is mediated by the C-termini of VPS35 subunits. This dimer particle structure

128   was very poorly resolved (18 Å average resolution) in previous studies (*40*). Others have

129   reported improvements in single particle structure determination by using a 3D starting model

130   (*46*) in early rounds of automated particle picking. We employed this strategy in RELION using

131   a previously obtained data set (*40*) and a 3D starting model filtered to 20 Å to gain additional

132   views of dimers in all possible orientations. We obtained an improved reconstruction (Figure 2A;

133   Figure S2) from 288,247 particles with an average resolution of 7.0 Å. The presence of

134   additional views substantially improved the structure (Figure 2E, 2F), although the N-terminal

135   end of one heterotrimer remains poorly resolved and overall resolution remains limited compared

136   to the heterotrimer (Figure 1).

137

138   Fitting rigid body models into Coulomb potential maps can be ambiguous, especially at modest

139   resolution. Therefore, we systematically analyzed map handedness in the improved dimer

140   reconstructions to generate the best model given the data. Briefly, we undertook the following

141   approach (*47*). Both the original and flipped maps were used to perform a global search in which

142   3,000 random orientations of the real space refined heterotrimer model (details in Methods) were

143   fitted as rigid bodies. A list of potential fits and cross-correlation coefficients were generated for

144   both maps (Figure S3A, D). Analyzing both maps with the top fitted model clearly demonstrated

145   the map with correct handedness (compare S3B, C with S3E, F).

146

147   *VPS35/VPS35 sub-structures*. Work from multiple labs has now demonstrated both yeast and

148   mammalian retromer form VPS35-mediated dimer interfaces in solution (*40, 45*) and when

149   assembled on membranes (*32, 33*). We re-visited two published sub-structures of VPS35/VPS35-

150   mediated dimers (*40*) to generate improved reconstructions. The first sub-structure (Figure 3A)

151   was determined from VPS35-mediated dimers observed in elongated retromer chains (*40*). The

152   second (Figure 3B) was determined from retromer dimers after employing a 3D starting model in

5

153   autopicking (previous section). The improved sub-structures revealed both interfaces are

154   asymmetrical (C1 symmetry; Figure S1) and place specific electrostatic residues directly in the

155   interface. These highly conserved residues (E615, D616, E617, K663, K701, K705) were

156   identified and tested in our previous work (*40*), and improved sub-structures presented here now

157   provide the highest resolution views of this critical VPS35-mediated assembly interface (see

158   Discussion).

159

160   *A new oligomeric interface mediated by VPS26A and VPS35.* One major limitation of our

161   previous study was an inability to resolve a new dimer interface found in chain links and

162   mediated by the N-terminus of VPS26 subunits (chain interface II in (*40*)). These elongated

163   chain particles exhibited extreme preferred orientation, so we used a published mutant that

164   breaks the VPS35/VPS35 dimer interface to generate a particle more tractable for cryo-EM

165   studies. This retromer "3KE" mutant (*40*) enriches the heterogeneous retromer protein sample

166   for particles that form dimers only at the VPS26 end. These smaller 3KE retromer mutant

167   particles resemble the "f-hole" found on the body of a violin (Figure 4). We obtained a tilted data

168   set from 3KE mutant retromer in the presence of a small cyclic peptide called RT-L4 (*44*), which

169   has been shown to stabilize retromer structure. The presence of this peptide further enriched our

170   protein sample for 3KE mutant particles. We generated a reconstruction of 3KE mutant dimers

171   (Figure 4A) from 40,957 particles using a 3D starting model (details in Methods) at an average

172   resolution of 7.1 Å. One heterotrimer in this particle appears better resolved than the other

173   (Figure 4C), which may reflect how the particle behaves at the air-water interface. The RT-L4

174   peptide is extremely hydrophobic, and 3KE particles with RT-L4 tend to exhibit preferred

175   orientation by aligning along the plane of the interface (Figure 4E). To better resolve the

176   interaction, we determined a sub-structure centered on the chain link from 19,386 particles at an

177   average resolution of 6.7 Å. Although one copy of N-VPS35 remains more poorly resolved

178   (Figure 4D), the sub-structure provides the first compelling view of this interface. The chain link

179   is mediated by a new interaction between the N-terminal arrestin saddle of VPS26 in one

180   heterotrimer with the N-terminus of VPS35 in a neighboring heterotrimer.

181

182   *Analysis of the N-VPS26 and N-VPS35 interface.* To further characterize the chain link interface,

183   buried surface area was calculated using PISA (*48*) (Figure 5). Within each retromer

184   heterotrimer, interactions between N-VPS35 and C-VPS26 (Figure 5A; black & grey hatched

185   circles) bury between 6,382 and 6,987 Å^2 (Figure 5B). For comparison, the buried surface

186   interface between N-VPS35 and C-VPS26 in the heterotrimer structure (Figure 1) is 6,178 Å^2.

187   The slightly larger buried surface area values for the equivalent interface in 3KE mutant particles

188   is consistent with RT-L4 playing a stabilizing role in this interface (*44*). The two new interfaces

189   are located on the opposite face of N-VPS35, where each N-VPS35 interacts with an N-VPS26

190   subunit from a neighboring molecule (Figure 5A; black and grey circles). Each new interface

191   buries around 7,000 Å^2 (Figure 5B). This analysis suggests the new interface buries

192   approximately the same amount of surface as the well-characterized interaction between N-

193   VPS35 and C-VPS26 within a retromer heterotrimer. The VPS35 N-terminal helix (residues 12-

194   36) interacts specifically with two VPS26A β-strands (residues 48-56; 105-111) and their

195   connecting loops (residues 56-63; 101-105) (Figure S6D, S6E). Like the C-terminal

196   VPS35/VPS35 interfaces (previous section), this N-VPS26/N-VPS35 interface does not exhibit

197   two-fold symmetry.

198

199   **Discussion**

200

201   *Improved data acquisition and image processing.* Two major improvements allowed us to

202   generate better reconstructions of retromer oligomers and to determine the structure of a new

203   interface. First, data acquisition from tilted specimens retrieved multiple and important missing

204   views for several structures, including retromer dimer and 3KE mutant particles. We previously

205   proposed the VPS35 subunit could exhibit flexibility along the length of its α-helical solenoid, as

206   judged by local resolution along the heterotrimer particle (*40*). However, the new reconstruction

207   (Figure 1) instead suggests the poor local resolution at the N-terminus was instead driven by

208   missing views. The decision to collect data from tilted specimens varies among practitioners, and

209   our experience points to the importance of considering this as a data collection strategy. The

210   second improvement arose from using a 3D starting model in early rounds of automated particle

211   picking. Use of the 3D starting model helps programs identify and include poorly sampled views,

212   and this was particularly effective in generating improved structures of retromer dimer and 3KE

213   mutant particles.

214

215   *C-VPS35 dimer interfaces.* The VPS35/VPS35 interface (Figure 3) we reported previously (*40*)

216   includes several important conserved electrostatic residues observed at the top of retromer arches

217   on membranes (*32, 33*). Both new sub-structures further support the placement of these residues

218   in the interface. The improved structures also reveal the interface is not two-fold symmetrical, in

219   agreement with reconstituted SNX3/retromer coats (*33*). We considered the possibility that

220   VPS35-mediated dimers of heterotrimers observed in vitreous ice might represent V-shaped

221   arches observed on membranes (*32, 33*). However, modelling arches into Coulomb potential

222   maps after ascertaining correct handedness (Figure S6A) does not support this. Extended

223   assemblies such as retromer dimers will likely be affected during sample blotting, so it is

224   possible that arches observed on membranes have been flattened during the plunge freezing

225   process by interactions at the air/water interface or by surface tension effects. Alternatively,

226   dimers may represent a more loosely associated retromer structure that is further organized when

227   it encounters relevant SNX proteins and cargoes on membranes.

228

229   *N-VPS26/N-VPS35 interface.* The interface between the N-termini of VPS35 and VPS26A was

230   previously observed in published structures of retromer chains (*40*) but is resolved more clearly

231   in this work (Figure 4) by using a retromer mutant that breaks the long chains into smaller

232   particles. The interface buries a substantial amount of surface area (nearly 7,000 $Å^2$), suggesting

233   it is a relatively stable particle *in vitro*. It is important to note this structure was determined in the

234   presence of RT-L4 (*44*), a small molecule shown to stabilize the N-VPS35/C-VPS26 interface.

235   The resolution of our structure is too low to locate or assign RT-L4, but in our hands, the

236   presence of RT-L4 appeared to increase the number of 3KE retromer particles observed on grids.

237   This suggests stabilizing the retromer heterotrimer in turn stabilized its ability to form the N-

238   VPS26A/N-VPS35 interface.

239

240   The resolution of both the 3KE particle structure and its sub-structure (~7 Å) are substantially

241   lower than the C-VPS35 interface sub-structure determined from chains (~4.5 Å). The limited

242   resolution makes it difficult to accurately identify specific residues mediating the interface with

243   high confidence since side chains cannot be assigned. Alpha-helices located in VPS35 interfaces

244   (Figure 3A, 3B) can be more confidently fit, compared to the VPS26 β-sheets in the 7 Å

245   resolution chain link sub-structure (Figure 4H). However, surface views of the interface suggest

246 the two N-termini are complementary in overall shape (Figure S6D, E). We also note the VPS26

247 N-terminal arrestin subdomain is less conserved than the C-terminal subdomain (Figure S6F)

248 (*39*), which may suggest retromer from different species cannot build this interface.

249

250 The biological relevance of the N-VPS26A/N-VPS35 interface remains unknown. It will be

251 important to test these structural models by mutating multiple residues along the interface to

252 ascertain whether disruption drives cargo sorting or other defects. In addition to endosomal

253 sorting, retromer has been implicated in other important cellular processes, including

254 mitochondrial derived vesicle formation (*49*) and regulation of mitochondrial membrane

255 integrity (*50*), as well as nutrient sensing (*51, 52*) and autophagy (*53*). How retromer regulates

256 mitochondrial morphology is unknown (*54*). Recent work (*55*) indicates a family of proteins

257 called PROPPINs can compete with SNX proteins for retromer binding under certain conditions,

258 and these PROPPIN-retromer interactions are linked to membrane fission events. Overall, the

259 diversity of potential metazoan retromer functions suggests retromer may also have expanded its

260 structural repertoire to assemble in different ways. This is not unprecedented, as other trafficking

261 proteins have been shown to assemble in different ways. One well-studied example is clathrin,

262 since clathrin on its own forms different lattices (*56*), and clathrin coated vesicles purified from

263 brain exhibit a variety of geometries (*57*). It will be interesting to determine whether and how

264 retromer may serve as a flexible scaffold to build different structures to mediate cellular events

265 under a variety of conditions.

266

267 **Materials & Methods**

268

269 *Reagents.* Unless otherwise noted, all chemicals were purchased from Fisher (Waltham, MA,

270 USA).

271

272 *Molecular biology and cloning.* Both wild-type (*38, 39*) and 3KE mutant (*40*) retromer

273 constructs have been published previously. Briefly, mouse VPS35 and VPS29 were placed in

274 vector pGEX4T2 (GE Healthcare), while VPS26 was placed in in-house vector pMWKan. A

275 two-stage quick-change mutagenesis protocol (*58*) was adapted to introduce three point

9

276   mutations (K659E/K662E/K663E) into the VPS35 subunit to generate the retromer "3KE"

277   electrostatic mutant that disrupts VPS35/VPS35 interface formation.

278

279   *Protein Expression and Purification.* Recombinant retromer protein (wild-type or 3KE mutant)

280   was expressed and purified from *E. coli* as previously described (*40*). Briefly, retromer plasmids

281   were transformed into BL21(DE3) Rosetta2 pLysS cells (Millipore). Cells were grown to an

282   OD_{600} between 0.8-1.0 and induced for 16-20 hours at 22°C with 0.4 mM IPTG. Cells were lysed

283   by a disruptor (Constant Systems). The protein was purified in 10 mM Tris-HCl (pH 8.0), 200

284   mM NaCl, 2 mM βME using Glutathione Sepharose (GE Healthcare). Protein was cleaved

285   overnight using thrombin (Recothrom, The Medicines Company) at room temperature and batch

286   eluted in buffer. Retromer was further purified by gel filtration on a Superdex S200 16/60

287   analytical column (GE Healthcare) into 10 mM Tris-HCl (pH 8.0), 200 mM NaCl, or dialyzed

288   into 20 mM HEPES pH 8.2, 50 mM NaCl, 2 mM DTT prior to vitrification.

289

290   *Negative Stain Grid Preparation & Screening.* For screening negatively stained retromer

291   samples, 10 ml of retromer at concentrations between 5 and 10 μg/mL were applied to

292   continuous carbon film on 400 square mesh copper EM grids (Electron Microscopy Sciences,

293   Hatfield, PA) and washed twice with water. The grids were stained with 2% uranyl formate and

294   1% uranyl acetate and air dried overnight. The grids were screened on a ThermoFisher Morgagni

295   microscope operating at 100 kV with an AMT 1Kx1K CCD camera (Center for Structural

296   Biology Cryo-EM Facility, Vanderbilt University) to verify protein quality.

297

298   *Cryo-EM sample preparation and data collection.*

299   *Grid preparation.* For cryo-electron microscopy, 2 μl retromer at a concentration between 80-

300   100 μg/ml was applied to freshly glow discharged CF-2/2-2C C-Flat grids (Protochips,

301   Morrisville, NC) or Quantifoil R 1.2/1.3 300 mesh copper grids (Quantifoil Micro Tools GmbH,

302   Großlöbichau, Germany). Grids were vitrified in liquid ethane using either a ThermoFisher

303   MarkIII or MarkIV Vitrobot, with blot times between 2-3.5 seconds and chamber conditions of

304   100% relative humidity and 8-20°C.

305

10

306   *Heterotrimer and flat substructure data collection.* Micrographs from three separate data

307   collections were used to generate the heterotrimer and flat substructure models. Each data

308   collection is summarized below and full details are also provided in Table 1. RELION-2 (*59*) and

309   RELION-3 (*60*) were used for all image processing unless otherwise indicated.

310

311   Data collection #1: 1480 micrographs were collected on a ThermoFisher Titan Krios microscope

312   at the National Resource for Automated Molecular Microscopy (NRAMM). The microscope

313   operated at 300 keV and was equipped with a Gatan BioQuantum energy filter with a slit width

314   of 20eV, a spherical aberration (Cs) corrector, and a Gatan K2 Summit direct electron detector

315   camera. The nominal magnification used during data collection was 105,000x, and the pixel size

316   was 1.096 Å/pix. The total electron dose was $69.34e^-/A^2$. Data collection was accomplished

317   using Leginon (*61*). Images were motion corrected using MotionCor2 (*62*). The CTF of each

318   micrograph was determined using Gctf (*63*); defocus values for the data varied between -0.7 and

319   -2.6 μm.

320

321   Data collection #2: 1299 micrographs were collected on a ThermoFisher Titan Krios microscope

322   at the National Resource for Automated Molecular Microscopy (NRAMM). The microscope

323   operated at 300 keV and was equipped with a Gatan BioQuantum energy filter with a slit width

324   of 20eV and a Gatan K2 Summit direct electron detector camera. The nominal magnification

325   used during data collection was 105,000x, and the pixel size was 1.06 Å/pix. The total electron

326   dose was $73.92e^-/A^2$. Data collection was accomplished using Leginon. Images were motion

327   corrected using MotionCor2, and micrographs from this data collection were rescaled to match

328   the 1.096Å/pix pixel size from the first data collection using an NRAMM script written for

329   MotionCor2. The CTF of each micrograph was determined using Gctf; defocus values for the

330   data varied between -0.8 and -4.4 μm.

331

332   Data collection #3: 891 micrographs were collected on a ThermoFisher Titan Krios microscope

333   at the National Resource for Automated Molecular Microscopy (NRAMM). The microscope

334   operated at 300 keV and was equipped with a Gatan BioQuantum energy filter with a slit width

335   of 20eV and a Gatan K2 Summit direct electron detector camera. The nominal magnification

336   used during data collection was 105,000x, and the pixel size was 1.06 Å/pix. The total electron

337   dose was 73.92e$^-$/A^2, and micrographs were collected at +/-15° tilts. Data collection was

338   accomplished using Leginon. Images were motion corrected using MotionCor2, and micrographs

339   from this data collection were rescaled to match the 1.096Å/pix pixel size from the first data

340   collection using an NRAMM script written for MotionCor2. The CTF of each micrograph was

341   determined using Gctf; defocus values for the data varied between -0.8 and -4.7μm.

342

343   *Dimer and dimer substructure data collection*. 1480 micrographs were collected on a

344   ThermoFisher Titan Krios microscope at the National Resource for Automated Molecular

345   Microscopy (NRAMM). The microscope operated at 300 keV and was equipped with a Gatan

346   BioQuantum energy filter with a slit width of 20eV and a Gatan K2 Summit direct electron

347   detector camera. The nominal magnification used during data collection was 105,000x, and the

348   pixel size was 1.096 Å/pix. The total electron dose was 69.34e$^-$/A^2. Data collection was

349   accomplished using Leginon. Images were motion corrected using MotionCor2. The CTF of

350   each micrograph was determined using Gctf; defocus values for the data varied between -0.7 and

351   -2.6μm. RELION-3 was used for all image processing unless otherwise indicated.

352

353   *Retromer 3KE mutant (f-hole) and sub-structure data collection.* 4791 micrographs were

354   collected on a ThermoFisher Titan Krios G3i microscope in the Center for Structural Biology's

355   Cryo-EM Facility at Vanderbilt. The microscope was operated at 300 keV and equipped with a

356   ThermoFisher Falcon3 direct electron detector camera. The nominal magnification used during

357   data collection was 120,000x, and the pixel size was 0.6811 Å/pix. The total electron dose was

358   50 e$^-$/A^2, and micrographs were collected at +/-30° tilts. Data collection was accomplished using

359   EPU (ThermoFisher). Images were motion corrected using MotionCor2. The CTF of each

360   micrograph was determined using Gctf; defocus values for the data varied between -0.8 and

361   -2.6 μm. RELION-3 was used for all image processing unless otherwise indicated.

362

363   _CryoEM data processing_

364   *Heterotrimer.* Data giving rise to our published retromer reconstruction (*40*) lacked tilted views;

365   an additional data set (data collection #3) was collected to add tilted views and to improve the

366   reconstruction for this study. Several thousand particles were manually selected from dataset #3

367   to perform initial 2D classification and produce templates for autopicking. Template-based

368 autopicking in RELION identified 207,026 particles, which were subjected to initial 2D and 3D

369 classification and refinement as well as CTF refinement. 250,500 particles from data collections

370 #1 and #2 were imported to combine with data collection #3. Multiple rounds of 2D

371 classification yielded 72,795 particles suitable to continue to 3D classification. Initial models for

372 3D classification were filtered to 60 Å resolution for use in these experiments. The particles

373 underwent multiple rounds of CTF refinement and Bayesian polishing to produce a final set of

374 43,808 particles suitable for 3D refinement and postprocessing. The final masked heterotrimer

375 model had a global resolution of 4.9 Å and a B-factor of -114 as determined in RELION.

376

377 *VPS35/VPS35 sub-structure from retromer chains.* Particles from the dataset containing all three

378 data collections were windowed to a smaller box size that centered on the 35/35 interaction

379 between two retromer molecules. Multiple rounds of 2D classification yielded 121,876 particles

380 suitable to continue to 3D classification. Initial models for 3D classification were filtered to 60 Å

381 resolution for use in these experiments. The particles underwent multiple rounds of CTF

382 refinement and Bayesian polishing to produce a final set of 69,381 particles suitable for 3D

383 refinement and postprocessing. The final masked flat substructure model had a global resolution

384 of 4.5Å and a B-factor of -226 as determined in RELION.

385

386 *Retromer dimers of trimers.* Several thousand particles were manually selected to perform initial

387 2D and 3D classifications. Micrographs were then autopicked using a 20 Å low-pass filtered 3D

388 model produced from initial rounds of manual picking; this template-based autopicking

389 identified 533,231 particles. Multiple rounds of 2D classification yielded 509,447 particles

390 suitable to continue to 3D classification. The same 3D model used for autopicking was filtered to

391 60 Å and used as an initial model for 3D classification. The particles underwent CTF refinement

392 to produce a final set of 208,247 particles suitable for 3D refinement. The final masked dimer

393 model had a global resolution of 7.0 Å, and no B-factor sharpening (postprocessing) was

394 performed in RELION. We generated a z-flipped model of the dimer in Chimera (*64*). We then

395 used the Chimera command "Fit in Map" to perform a global search testing 3000 random

396 orientations of our real space refined heterotrimer model filtered to 7 Å, with random

397 displacement of 5Å into each map. We generated a list of possible fits with cross-correlations for

398 both the z-flipped and unflipped maps of the dimer.

13

399

400 *Dimer substructure.* The particles contained in the refined set from the full dimer were

401 windowed to a smaller box size that centered on the VPS35/VPS35 interaction between two

402 retromer molecules. Multiple rounds of 2D classification yielded 288,246 particles suitable to

403 continue to 3D classification. A windowed model of the refined full dimer structure was filtered

404 to 60 Å and used as an initial model for 3D classification. A set of 268,764 particles continued to

405 3D refinement, and the final masked dimer substructure model had a resolution of 6.5 Å; no B-

406 factor sharpening (postprocessing) was performed in RELION.

407

408 *Retromer 3KE mutant (f-hole).* Micrographs were autopicked using a 20 Å low-pass filtered 3D

409 model that had been produced in early rounds of processing, and this template-based autopicking

410 identified 275,633 particles. Multiple rounds of 2D classification yielded 154,553 particles

411 suitable to continue to 3D classification. The same 3D model used for autopicking was filtered to

412 60 Å and used as an initial model for 3D classification. The particles underwent CTF refinement

413 to produce a final set of 40,957 particles suitable for 3D refinement. The final masked model

414 exhibited a resolution of 7.1 Å; no B-factor sharpening (postprocessing) was performed in

415 RELION. To analyze map handedness, a z-flipped model of the retromer 3KE particle was

416 generated in Chimera (Pettersen et al., 2004). We performed a global search testing 3,000

417 random orientations of the real space refined heterotrimer model (VPS26/VPS35/VPS29 as a

418 single rigid body) filtered to 7 Å using the Chimera command "Fit in Map", with random

419 displacement of 5 Å into each map. This approach generated a list of potential fits with cross-

420 correlations for both maps. Analyzing both maps with fitted rigid body models in Chimera

421 clearly demonstrated the map with correct handedness.

422

423 *Retromer 3KE (f-hole) substructure.* The particles contained in the refined set from the full F-

424 hole were windowed to a smaller box size that centered on the 35/26 tails of the two retromer

425 molecules. Multiple rounds of 2D classification yielded 19,386 particles suitable to continue to

426 3D classification. A windowed model of the refined full f-hole structure was filtered to 60Å and

427 used as an initial model for 3D classification. A set of 40,957 particles continued to 3D

428 refinement, and the final masked f-hole substructure model had a resolution of 6.7Å; no B-factor

429 sharpening (postprocessing) was performed in RELION.

14

430   *Model Building & Docking.* Models for VPS29 and the VPS35 C-terminus were obtained from

431   PDB 2R17, while models for N-VPS35 and VPS26A were obtained from PDB 5F0J. We omitted

432   a flexible unstructured loop (amino acids 470-482) that is absent in all crystal structures. Rigid-

433   body docking and map visualization were performed in Chimera using the command "Fit in

434   Map".

435

436   *Retromer heterotrimer map sharpening.* We used the 5 Å resolution Coulomb potential map to

437   refine an atomic model of retromer. The Coulomb potential map was further postprocessed in

438   PHENIX by performing global or local B factor sharpening using the program "Auto-

439   sharpening" with a resolution cut-off at 5 Å. A PDB model containing all three retromer subunits

440   (VPS26 and VPS35 from PDB: 5F0J; VPS29 from PDB: 2R17)was docked into the sharpened

441   map and traced manually in Coot. Subsequently, several rounds of real space refinement were

442   performed in PHENIX (*65*). Overall statistics and geometry for the final model were analyzed

443   using MolProbity (*66, 67*) and are summarized in Table 2. The overall root-mean-square

444   deviation (RMSD) between C_α atoms in the refined versus starting models was 1.1 Å. However,

445   the overall geometric parameters of C_α atoms are improved in the new model, suggesting the side

446   chains likely occupy more favorable conformations in the new model. While overall

447   improvements in the model appear relatively small, the overall improvement in the sharpened

448   map is substantial, showing that with current tools a cryo-EM map of modest quality at 5 Å

449   resolution can be used to generate a fairly reliable model (Figure 1).

450

451   *Data visualization.* All figures were generated using CCP4MG (*68*) or Chimera (*64*).

452

453   *Data deposition.* Coulomb potential maps were deposited in the EMDB with accession numbers

454   EMD-24964, EMD-26342, and EMD-26341, corresponding to retromer heterotrimer; dimers;

455   and 3KE mutant particles. Sub-structure maps were deposited for C-VPS35 dimers as EMD-

456   26343 and EMD-26345, and for the 3KE mutant as EMD-26340. The heterotrimer data set was

457   first reported very briefly in (*44*), but its refinement and analysis are reported here. Coordinates

458   for this updated retromer heterotrimer were deposited in the Protein Data Bank as XXXX.

459

460

15

Acknowledgements

References

1. M. N. Seaman, J. M. McCaffery, S. D. Emr, A Membrane Coat Complex Essential for Endosome-to-Golgi Retrograde Transport in Yeast. *J Cell Biol*. **142**, 665–81 (1998).

2. M. N. J. Seaman, Cargo-selective endosomal sorting for retrieval to the Golgi requires retromer. *J Cell*. **165**, 111–22 (2004).

3. C. N. Arighi, L. M. Hartnell, R. C. Aguilar, C. R. Haft, J. S. Bonifacino, Role of the mammalian retromer in sorting of the cation-independent mannose 6-phosphate receptor. *J. Cell Biol.* **165**, 123–33 (2004).

4. B. E. L. Lauffer, C. Melero, P. Temkin, C. Lei, W. Hong, T. Kortemme, M. von Zastrow, SNX27 mediates PDZ-directed sorting from endosomes to the plasma membrane. *J Cell Biol*. **190**, 565–74 (2010).

5. P. Temkin, B. Lauffer, S. Jäger, P. Cimermancic, N. J. Krogan, M. von Zastrow, SNX27 mediates retromer tubule entry and endosome-to-plasma membrane trafficking of signalling receptors. *Nat. Cell Biol*. **13**, 715–21 (2011).

6. F. Steinberg, M. Gallon, M. Winfield, E. C. Thomas, A. J. Bell, K. J. Heesom, J. M. Tavaré, P. J. Cullen, A global analysis of SNX27-retromer assembly and cargo specificity reveals a function in glucose and metal ion transport. *Nat Cell Biol*. **15**, 461–71 (2013).

7. R. W.-Y. Choy, M. Park, P. Temkin, B. E. Herring, A. Marley, R. A. Nicoll, M. von Zastrow, Retromer mediates a discrete route of local membrane delivery to dendrites. *Neuron*. **82**, 55–62 (2014).

8. C. G. Burd, P. J. Cullen, Retromer: a master conductor of endosome sorting. *Cold Spring Harb Perspect Biol*. **6** (2014), doi:10.1101/cshperspect.a016774.

9. B. Simonetti, P. J. Cullen, Endosomal Sorting: Architecture of the Retromer Coat. *Curr. Biol.* **28**, R1350–R1352 (2018).

10. M. Chandra, A. K. Kendall, L. P. Jackson, Toward Understanding the Molecular Role of SNX27/Retromer in Human Health and Disease. *Front. Cell Devel Biol*. **9**, 642378 (2021).

11. L. Lu, W. Hong, From endosomes to the trans-Golgi network. *Sem Cell Dev Biol*. **31**, 30–9 (2014).

12. A. Fjorback, M. Seaman, C. Gustafsen, A. Mehmedbasic, S. Gokool, C. Wu, D. Militz, V. Schmidt, P. Madsen, Nyengaard, T. Willnow, E. Christensen, W. Mobley, A. Nykjær, O.

505   Andersen, Retromer binds the FANSHY sorting motif in SorLA to regulate amyloid
506   precursor protein sorting and processing. *J Neurosci*. **32**, 1467–80 (2012).

507 13. O. M. Andersen, J. Reiche, V. Schmidt, M. Gotthardt, R. Spoelgen, J. Behlke, C. A. F.
508   von Arnim, T. Breiderhoff, P. Jansen, X. Wu, K. R. Bales, R. Cappai, C. L. Masters, J.
509   Gliemann, E. J. Mufson, B. T. Hyman, S. M. Paul, A. Nykjaer, T. E. Willnow, Neuronal
510   sorting protein-related receptor sorLA/LR11 regulates processing of the amyloid precursor
511   protein. *Proc Natl Acad Sci U S A*. **102**, 13461–6 (2005).

512 14. J. Yin, X. Liu, Q. He, L. Zhou, Z. Yuan, S. Zhao, Vps35-dependent recycling of Trem2
513   regulates microglial function. *Traffic*. **17**, 1286–1296 (2016).

514 15. C. Reitz, S. Tokuhiro, L. N. Clark, C. Conrad, J.-P. Vonsattel, L.-N. Hazrati, A. Palotás,
515   R. Lantigua, M. Medrano, I. Z. Jiménez -Velázquez, B. Vardarajan, I. Simkin, J. L.
516   Haines, M. A. Pericak -Vance, L. A. Farrer, J. H. Lee, E. Rogaeva, P. St. George- Hyslop,
517   R. Mayeux, SORCS1 alters amyloid precursor protein processing and variants may
518   increase Alzheimer's disease risk. *Ann. Neurol.* **69**, 47–64 (2011).

519 16. V. J. Mecozzi, D. E. Berman, S. Simoes, C. Vetanovetz, M. R. Awal, V. M. Patel, R. T.
520   Schneider, G. a Petsko, D. Ringe, S. a Small, Pharmacological chaperones stabilize
521   retromer to limit APP processing. *Nat Chem Biol*. **10**, 443–9 (2014).

522 17. S. A. Small, K. Kent, A. Pierce, C. Leung, M. S. Kang, H. Okada, L. Honig, J.-P.
523   Vonsattel, T.-W. Kim, Model-guided microarray implicates the retromer complex in
524   Alzheimer's disease. *Ann. Neurol.* **58**, 909–19 (2005).

525 18. A. Zimprich, A. Benet-Pagès, W. Struhal, E. Graf, S. H. Eck, M. N. Offman, D.
526   Haubenberger, S. Spielberger, E. C. Schulte, P. Lichtner, S. C. Rossle, N. Klopp, E. Wolf,
527   K. Seppi, W. Pirker, S. Presslauer, B. Mollenhauer, R. Katzenschlager, T. Foki, C. Hotzy,
528   E. Reinthaler, A. Harutyunyan, R. Kralovics, A. Peters, F. Zimprich, T. Brücke, W.
529   Poewe, E. Auff, C. Trenkwalder, B. Rost, G. Ransmayr, J. Winkelmann, T. Meitinger, T.
530   M. Strom, A mutation in VPS35, encoding a subunit of the retromer complex, causes late-
531   onset Parkinson disease. *Am J Hum Genet*. **89**, 168–75 (2011).

532 19. M. E. Curtis, D. Yu, D. Praticò, Dysregulation of the Retromer Complex System in Down
533   Syndrome. *Ann. Neurol.* **88**, 137–147 (2020).

534 20. A. Filippone, D. Praticò, Endosome Dysregulation in Down Syndrome: A Potential
535   Contributor to Alzheimer Disease Pathology. *Ann. Neurol.* **90**, 4–14 (2021).

536   21.   M. Romano-Moreno, A. L. Rojas, C. D. Williamson, D. C. Gershlick, M. Lucas, M. N.

537   Isupov, J. S. Bonifacino, M. P. Machner, A. Hierro, Molecular mechanism for the

538   subversion of the retromer coat by the Legionella effector RidL. *Proc Natl Acad Sci U S*

539   *A*. **114**, E11151–E11160 (2017).

540   22.   Z. Daniloski, T. X. Jordan, H.-H. Wessels, D. A. Hoagland, S. Kasela, M. Legut, S.

541   Maniatis, E. P. Mimitou, L. Lu, E. Geller, O. Danziger, B. R. Rosenberg, H. Phatnani, P.

542   Smibert, T. Lappalainen, B. R. TenOever, N. E. Sanjana, Identification of Required Host

543   Factors for SARS-CoV-2 Infection in Human Cells. *Cell*. **184**, 92-105.e16 (2021).

544   23.   E. Sztul, P.-W. Chen, J. E. Casanova, J. Cherfils, J. B. Dacks, D. G. Lambright, F.-J. S.

545   Lee, P. A. Randazzo, L. C. Santy, A. Schürmann, I. Wilhelmi, M. E. Yohe, R. A. Kahn,

546   ARF GTPases and their GEFs and GAPs: concepts and challenges. *Mol. Biol. Cell*. **30**,

547   1249–1271 (2019).

548   24.   M. Chandra, A. K. Kendall, L. P. Jackson, Unveiling the cryo-EM structure of retromer.

549   *Biochem. Soc. Trans.* **48** (2020), doi:10.1042/BST20200552.

550   25.   C. N. Arighi, L. M. Hartnell, R. C. Aguilar, C. R. Haft, J. S. Bonifacino, Role of the

551   mammalian retromer in sorting of the cation-independent mannose 6-phosphate receptor.

552   *J Cell Biol*. **165**, 123–33 (2004).

553   26.   S. F. Nothwehr, S. A. Ha, P. Bruinsma, Sorting of yeast membrane proteins into an

554   endosome-to-Golgi pathway involves direct interaction of their cytosolic domains with

555   Vps35p. *J Cell Biol*. **151**, 297–309 (2000).

556   27.   A. Kvainickas, A. Jimenez-Orgaz, H. Nägele, Z. Hu, J. Dengjel, F. Steinberg, Cargo-

557   selective SNX-BAR proteins mediate retromer trimer independent retrograde transport. *J*

558   *Cell Biol*. **216**, 3677–3693 (2017).

559   28.   B. Simonetti, B. Paul, K. Chaudhari, S. Weeratunga, F. Steinberg, M. Gorla, K. J.

560   Heesom, G. J. Bashaw, B. M. Collins, P. J. Cullen, Molecular identification of a BAR

561   domain-containing coat complex for endosomal recycling of transmembrane proteins. *Nat*

562   *Cell Biol*. **21**, 1219–1233 (2019).

563   29.   M. S. Harrison, C.-S. Hung, T. Liu, R. Christiano, T. C. Walther, C. G. Burd, A

564   mechanism for retromer endosomal coat complex assembly with cargo. *Proc Natl Acad*

565   *Sci U S A*. **111**, 267–72 (2014).

566   30.   B. D. M. Bean, M. Davey, E. Conibear, Cargo selectivity of yeast sorting nexins. *Traffic*.

567   **18**, 110–122 (2017).

568   31.   M. Lucas, D. C. Gershlick, A. Vidaurrazaga, A. L. Rojas, J. S. Bonifacino, A. Hierro,

569   Structural Mechanism for Cargo Recognition by the Retromer Complex. *Cell*. **167**, 1623-

570   1635.e14 (2016).

571   32.   O. Kovtun, N. Leneva, Y. S. Bykov, N. Ariotti, R. D. Teasdale, M. Schaffer, B. D. Engel,

572   D. J. Owen, J. A. G. Briggs, B. M. Collins, Structure of the membrane-assembled retromer

573   coat determined by cryo-electron tomography. *Nature*. **561**, 561–564 (2018).

574   33.   N. Leneva, O. Kovtun, D. R. Morado, J. A. G. Briggs, D. J. Owen, Architecture and

575   mechanism of metazoan retromer:SNX3 tubular coat assembly. *Sci. Adv.* **7** (2021),

576   doi:10.1126/sciadv.abf8598.

577   34.   J. Carlton, M. Bujny, B. J. Peter, V. M. J. Oorschot, A. Rutherford, H. Mellor, J.

578   Klumperman, H. T. McMahon, P. J. Cullen, Sorting nexin-1 mediates tubular endosome-

579   to-TGN transport through coincidence sensing of high- curvature membranes and 3-

580   phosphoinositides. *Curr Biol*. **14**, 1791–800 (2004).

581   35.   B. Simonetti, C. M. Danson, K. J. Heesom, P. J. Cullen, Sequence-dependent cargo

582   recognition by SNX-BARs mediates retromer-independent transport of CI-MPR. *J Cell*

583   *Biol*. **216**, 3695–3712 (2017).

584   36.   T. I. Strochlic, T. G. Setty, A. Sitaram, C. G. Burd, Grd19/Snx3p functions as a cargo-

585   specific adapter for retromer-dependent endocytic recycling. *J Cell Biol*. **177**, 115–25

586   (2007).

587   37.   A. Hierro, A. L. Rojas, R. Rojas, N. Murthy, G. Effantin, A. V Kajava, A. C. Steven, J. S.

588   Bonifacino, J. H. Hurley, Functional architecture of the retromer cargo-recognition

589   complex. *Nature*. **449**, 1063–7 (2007).

590   38.   B. M. Collins, C. F. Skinner, P. J. Watson, M. N. Seaman, D. J. Owen, Vps29 has a

591   phosphoesterase fold that acts as a protein interaction scaffold for retromer assembly. *Nat*

592   *Struct Mol Biol*. **12**, 594–602 (2005).

593   39.   B. M. Collins, S. J. Norwood, M. C. Kerr, D. Mahony, M. N. J. Seaman, R. D. Teasdale,

594   D. J. Owen, Structure of Vps26B and mapping of its interaction with the retromer protein

595   complex. *Traffic*. **9**, 366–79 (2008).

596   40.   A. K. Kendall, B. Xie, P. Xu, J. Wang, R. Burcham, M. N. Frazier, E. Binshtein, H. Wei,

597   T. R. Graham, T. Nakagawa, L. P. Jackson, Mammalian Retromer Is an Adaptable

598   Scaffold for Cargo Sorting from Endosomes. *Structure*. **28**, 393-405.e4 (2020).

599 41.   H. Shi, R. Rojas, J. S. Bonifacino, J. H. Hurley, The retromer subunit Vps26 has an

600   arrestin fold and binds Vps35 through its C-terminal domain. *Nat Struct Mol Biol*. **13**,

601   540–548 (2006).

602 42.   K. E. McNally, R. Faulkner, F. Steinberg, M. Gallon, R. Ghai, D. Pim, P. Langton, N.

603   Pearson, C. M. Danson, H. Nägele, L. L. Morris, A. Singla, B. L. Overlee, K. J. Heesom,

604   R. Sessions, L. Banks, B. M. Collins, I. Berger, D. D. Billadeau, E. Burstein, P. J. Cullen,

605   Retriever is a multiprotein complex for retromer-independent endosomal cargo recycling.

606   *Nat Cell Biol*. **19**, 1214–1225 (2017).

607 43.   D. Wang, M. Guo, Z. Liang, J. Fan, Z. Zhu, J. Zang, X. Li, M. Teng, L. Niu, Y. Dong, P.

608   Liu, Crystal structure of human vacuolar protein sorting protein 29 reveals a

609   phosphodiesterase/nuclease-like fold and two protein-protein interaction sites. *J Biol*

610   *Chem*. **280**, 22962–22967 (2005).

611 44.   K.-E. Chen, Q. Guo, T. A. Hill, Y. Cui, A. K. Kendall, Z. Yang, R. J. Hall, M. D. Healy, J.

612   Sacharz, S. J. Norwood, S. Fonseka, B. Xie, R. C. Reid, N. Leneva, R. G. Parton, R. Ghai,

613   D. A. Stroud, D. P. Fairlie, H. Suga, L. P. Jackson, R. D. Teasdale, T. Passioura, B. M.

614   Collins, De novo macrocyclic peptides for inhibiting, stabilizing, and probing the function

615   of the retromer endosomal trafficking complex. *Sci. Adv.* **7**, eabg4007 (2021).

616 45.   S. J. Norwood, D. J. Shaw, N. P. Cowieson, D. J. Owen, R. D. Teasdale, B. M. Collins,

617   Assembly and solution structure of the core retromer protein complex. *Traffic*. **12**, 56–71

618   (2010).

619 46.   B. J. Greber, J. Remis, S. Ali, E. Nogales, 2.5 Å-resolution structure of human CDK-

620   activating kinase bound to the clinical inhibitor ICEC0942. *Biophys. J.* **120**, 677–686

621   (2021).

622 47.   W. Wan, L. Kolesnikova, M. Clarke, A. Koehler, T. Noda, S. Becker, J. A. G. Briggs,

623   Structure and assembly of the Ebola virus nucleocapsid. *Nature*. **551**, 394–397 (2017).

624 48.   E. Krissinel, K. Henrick, Inference of macromolecular assemblies from crystalline state. *J*

625   *Mol Biol*. **372**, 774–797 (2007).

626 49.   E. Braschi, V. Goyon, R. Zunino, A. Mohanty, L. Xu, H. M. McBride, Vps35 mediates

627   vesicle transport between the mitochondria and peroxisomes. *Curr Biol*. **20**, 1310–1315

628   (2010).

629   50.   T. Farmer, K. L. O'Neill, N. Naslavsky, X. Luo, S. Caplan, Retromer facilitates the
630   localization of Bcl-xL to the mitochondrial outer membrane. *Mol Biol Cell*. **30**, 1138–
631   1146 (2019).

632   51.   A. Kvainickas, H. Nägele, W. Qi, L. Dokládal, A. Jimenez-Orgaz, L. Stehl, D. Gangurde,
633   Q. Zhao, Z. Hu, J. Dengjel, C. De Virgilio, R. Baumeister, F. Steinberg, Retromer and
634   TBC1D5 maintain late endosomal RAB7 domains to enable amino acid-induced
635   mTORC1 signaling. *J Cell Biol*. **218**, 3019–3038 (2019).

636   52.   G. G. Hesketh, F. Papazotos, J. Pawling, D. Rajendran, J. D. R. Knight, S. Martinez, M.
637   Taipale, D. Schramek, J. W. Dennis, A.-C. Gingras, The GATOR-Rag GTPase pathway
638   inhibits mTORC1 activation by lysosome-derived amino acids. *Science (80-.)*. **370**, 351–
639   356 (2020).

640   53.   S. Roy, A. M. Leidal, J. Ye, S. M. Ronen, J. Debnath, Autophagy-Dependent Shuttling of
641   TBC1D5 Controls Plasma Membrane Translocation of GLUT1 and Glucose Uptake. *Mol*
642   *Cell*. **67**, 84-95.e5 (2017).

643   54.   T. Farmer, N. Naslavsky, S. Caplan, Tying trafficking to fusion and fission at the mighty
644   mitochondria. *Traffic*. **19**, 569–577 (2018).

645   55.   T. Courtellemont, M. G. De Leo, N. Gopaldass, A. Mayer, *bioRxiv*, in press,
646   doi:10.1101/2021.09.06.459059.

647   56.   K. L. Morris, J. R. Jones, M. Halebian, S. Wu, M. Baker, J.-P. Armache, A. Avila Ibarra,
648   R. B. Sessions, A. D. Cameron, Y. Cheng, C. J. Smith, Cryo-EM of multiple cage
649   architectures reveals a universal mode of clathrin self-assembly. *Nat Struct Mol Biol*. **26**,
650   890–898 (2019).

651   57.   M. Paraan, J. Mendez, S. Sharum, D. Kurtin, H. He, S. M. Stagg, The structures of
652   natively assembled clathrin-coated vesicles. *Sci. Adv.* **6**, eaba8397 (2020).

653   58.   W. Wang, B. A. Malcolm, Two-stage PCR protocol allowing introduction of multiple
654   mutations, deletions and insertions using QuikChange Site-Directed Mutagenesis.
655   *Biotechniques*. **26**, 680–682 (1999).

656   59.   S. H. W. Scheres, RELION: implementation of a Bayesian approach to cryo-EM structure
657   determination. *J Struct Biol*. **180**, 519–30 (2012).

658   60.   J. Zivanov, T. Nakane, B. O. Forsberg, D. Kimanius, W. J. Hagen, E. Lindahl, S. H.
659   Scheres, New tools for automated high-resolution cryo-EM structure determination in

660   RELION-3. *Elife*. **7** (2018), doi:10.7554/eLife.42166.

661   61.   B. Carragher, N. Kisseberth, D. Kriegman, R. A. Milligan, C. S. Potter, J. Pulokas, A.

662   Reilein, Leginon: an automated system for acquisition of images from vitreous ice

663   specimens. *J Struct Biol*. **132**, 33–45 (2000).

664   62.   S. Q. Zheng, E. Palovcak, J.-P. Armache, K. A. Verba, Y. Cheng, D. A. Agard,

665   MotionCor2: anisotropic correction of beam-induced motion for improved cryo-electron

666   microscopy. *Nat. Methods*. **14**, 331–332 (2017).

667   63.   K. Zhang, Gctf: Real-time CTF determination and correction. *J Struct Biol*. **193**, 1–12

668   (2016).

669   64.   E. F. Pettersen, T. D. Goddard, C. C. Huang, G. S. Couch, D. M. Greenblatt, E. C. Meng,

670   T. E. Ferrin, UCSF Chimera--a visualization system for exploratory research and analysis.

671   *J Comp Chem*. **25**, 1605–12 (2004).

672   65.   P. D. Adams, P. V Afonine, G. Bunkóczi, V. B. Chen, I. W. Davis, N. Echools, J. J.

673   Headd, L.-W. Hung, G. J. Kapral, R. W. Grosse-Kunstleve, A. J. McCoy, N. W. Moriarty,

674   R. Oeffner, R. J. Read, D. C. Richardson, J. S. Richardson, T. C. Terwilliger, P. H. Zwart,

675   PHENIX: a comprehensive, Python-based system for macromolecular structure solution.

676   *Acta Cryst D*. **66**, 213–221 (2010).

677   66.   V. B. Chen, W. B. Arendall, J. J. Headd, D. A. Keedy, R. M. Immormino, G. J. Kapral, L.

678   W. Murray, J. S. Richardson, D. C. Richardson, MolProbity: all-atom structure validation

679   for macromolecular crystallography. *Acta Cryst D*. **66**, 12–21 (2010).

680   67.   C. J. Williams, J. J. Headd, N. W. Moriarty, M. G. Prisant, L. L. Videau, L. N. Deis, V.

681   Verma, D. A. Keedy, B. J. Hintze, V. B. Chen, S. Jain, S. M. Lewis, W. B. Arendall, J.

682   Snoeyink, P. D. Adams, S. C. Lovell, J. S. Richardson, D. C. Richardson, MolProbity:

683   More and better reference data for improved all-atom structure validation. *Pro Sci*. **27**,

684   293–315 (2018).

685   68.   S. McNicholas, E. Potterton, K. S. Wilson, M. E. M. Noble, Presenting your structures:

686   the CCP4mg molecular-graphics software. *Acta Cryst D*. **67**, 386–94 (2011).

687
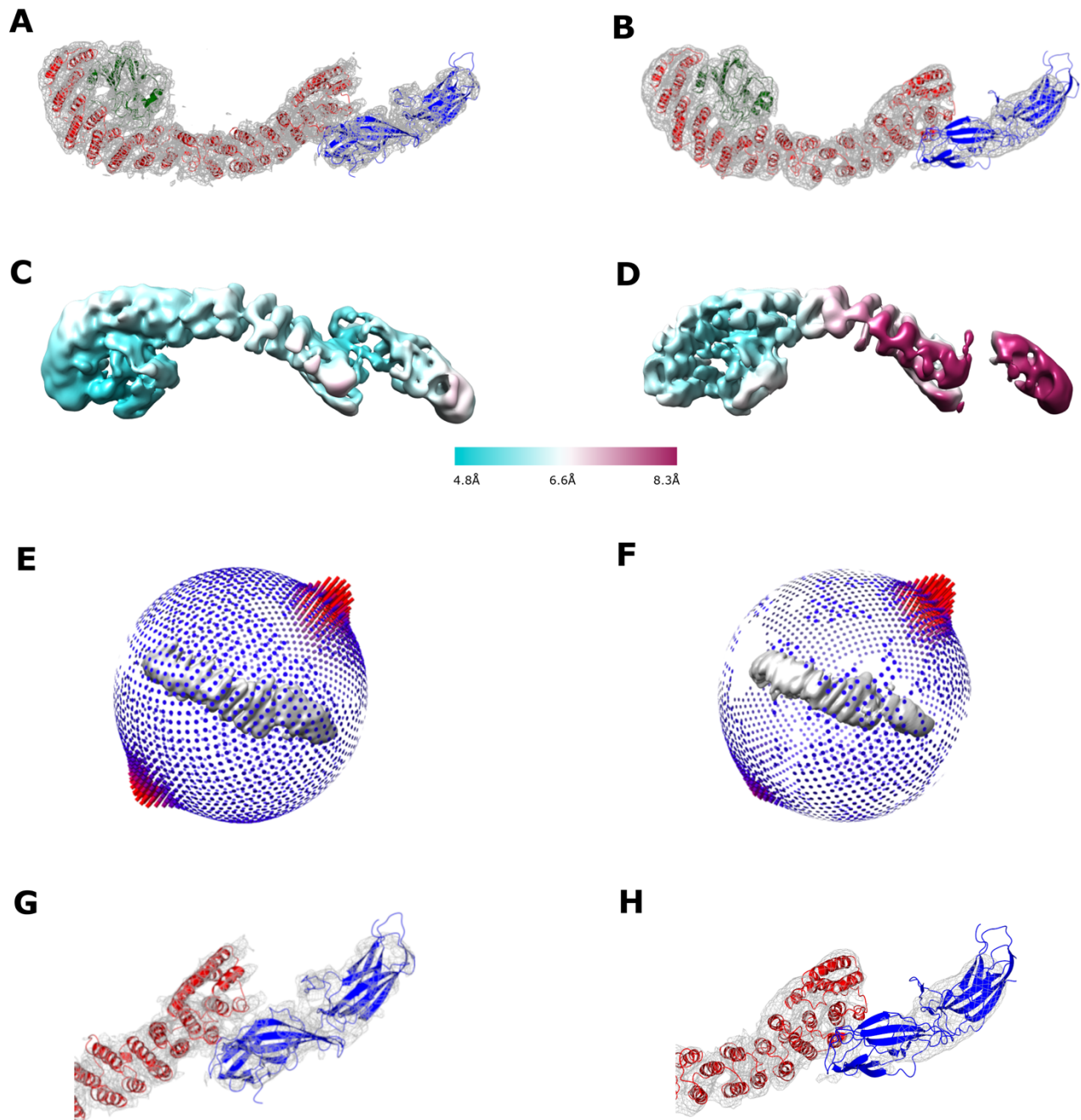
Figure 1. Single particle reconstructions of the mammalian retromer heterotrimer. (A, B) Comparison of new 4.9 Å resolution (A) and previously reported (B) reconstructions of retromer heterotrimer with fitted models. VPS29 is shown as green ribbons, VPS35 as red ribbons, and VPS26 as blue ribbons. (C, D) Local resolution comparisons across new (C) and reported (D) heterotrimer reconstructions. (E, F) Angular distribution in new (E) and reported (F) reconstructions. (G, H) Close-up views of N-VPS35/C-VPS26 interface in new (G) and reported (H) reconstructions. All Coulomb potential maps were generated using CCP4MG and are shown at 5σ contour level. Overall, acquisition of tilt data and improvements in data processing (details in text) resulted in an improved model.
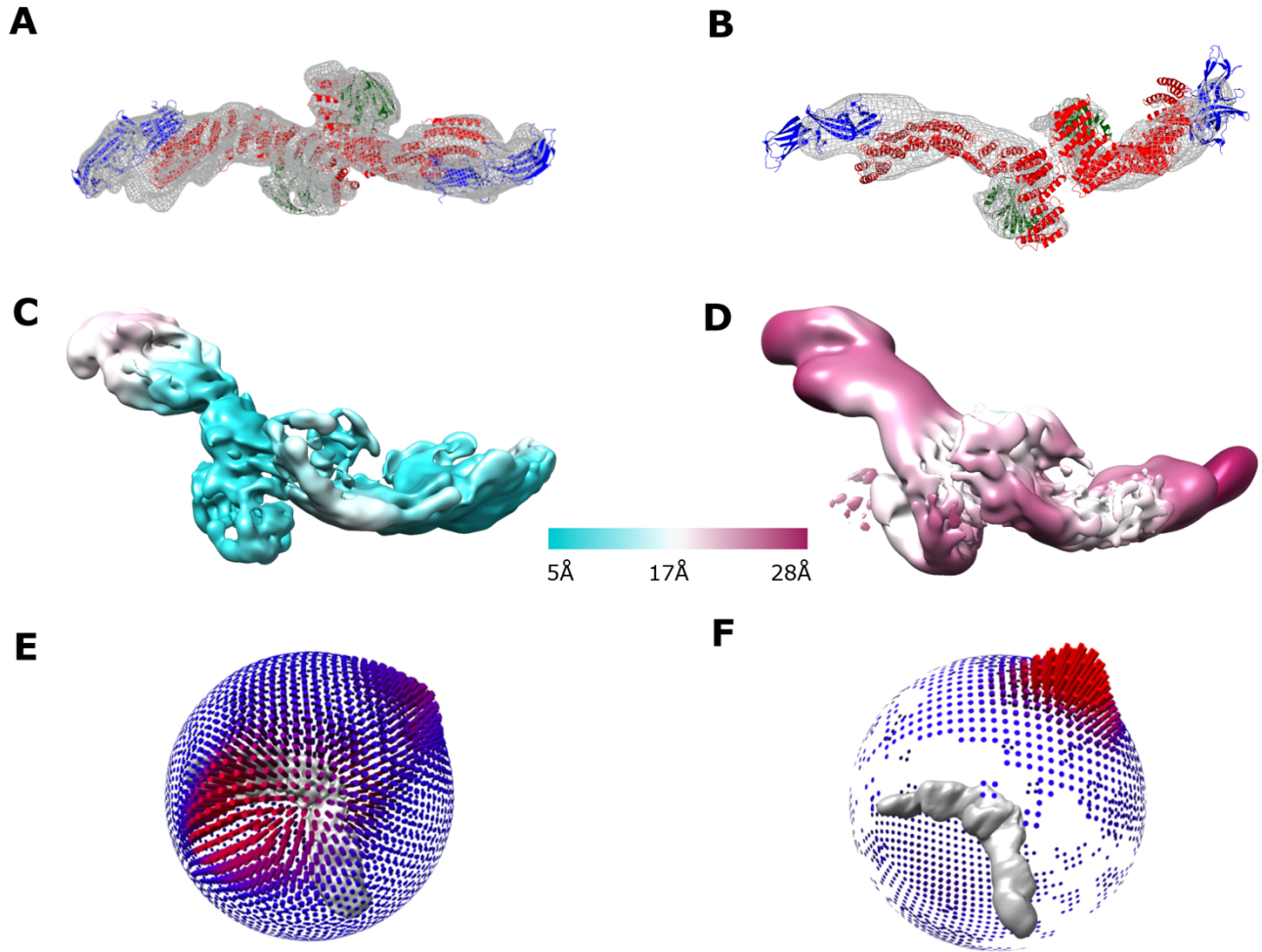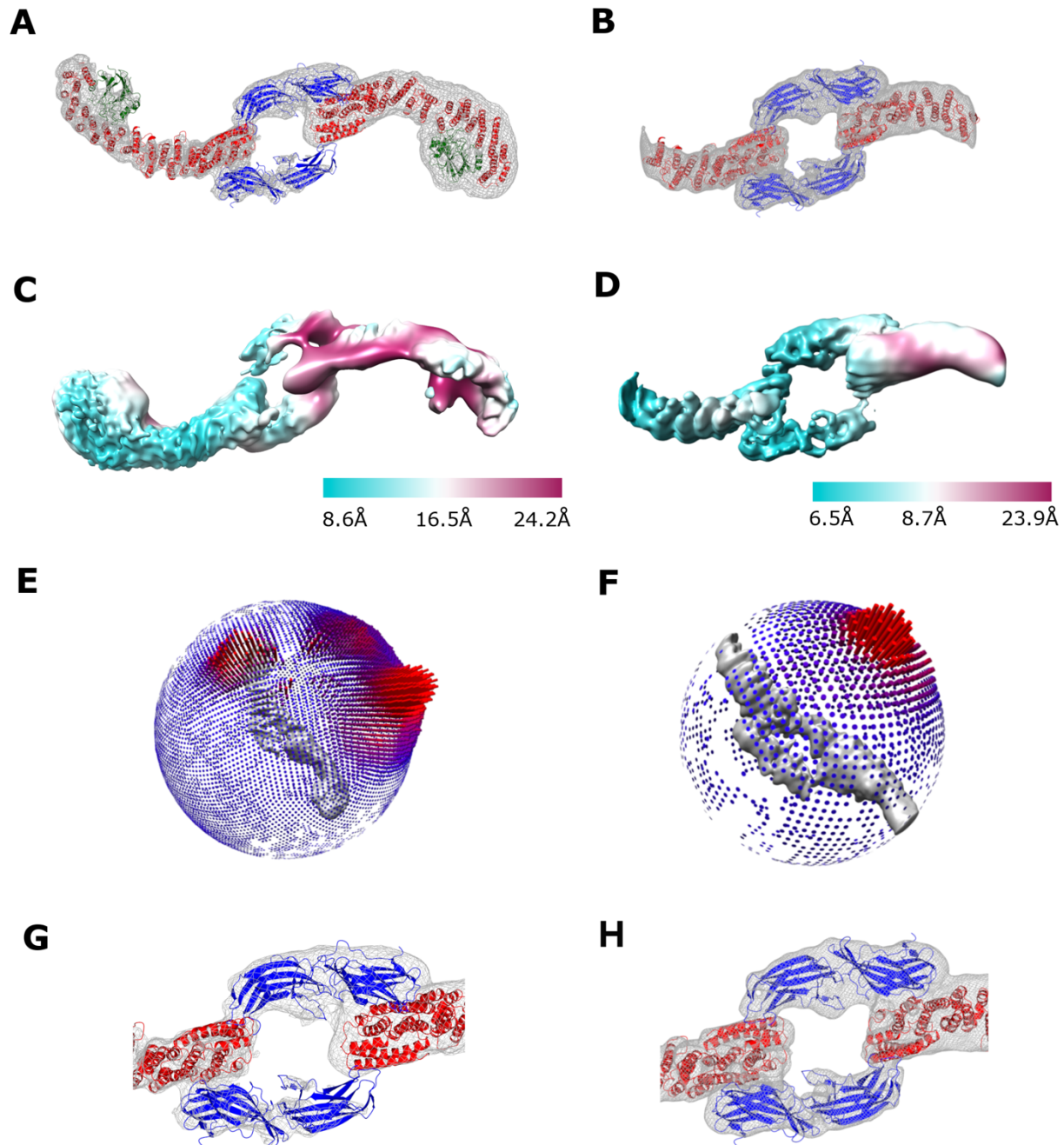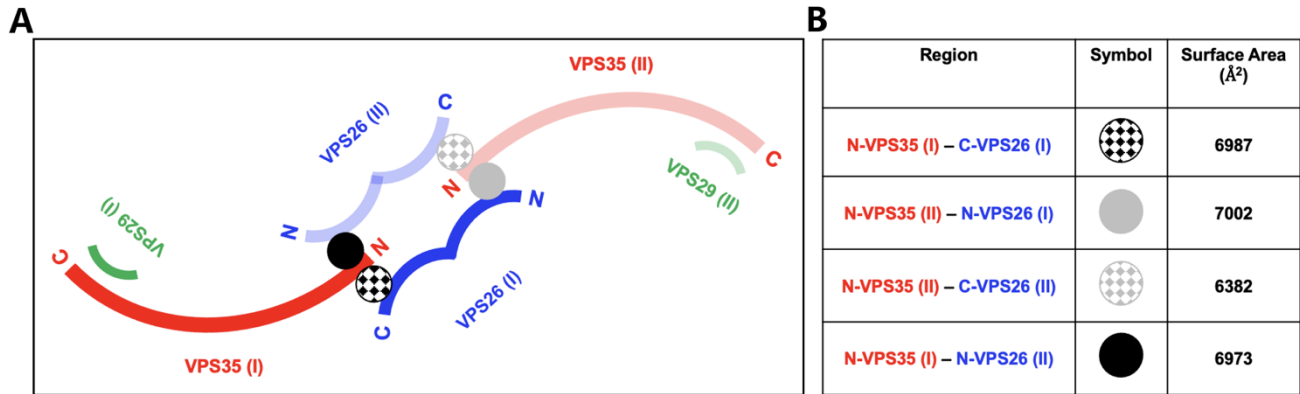
Figure 2. Single particle reconstructions of retromer dimers of trimers. (A, B) Comparison of new (A) and previously reported (B) reconstructions of retromer dimers of heterotrimers with fitted models. Coulomb potential maps generated using CCP4MG are shown at 6σ (A) and 4σ (B) contour levels, respectively. (C, D) Local resolution comparisons across new (C) and reported (D) reconstructions. (E, F) Angular distribution in new (E) and reported (F) reconstructions.
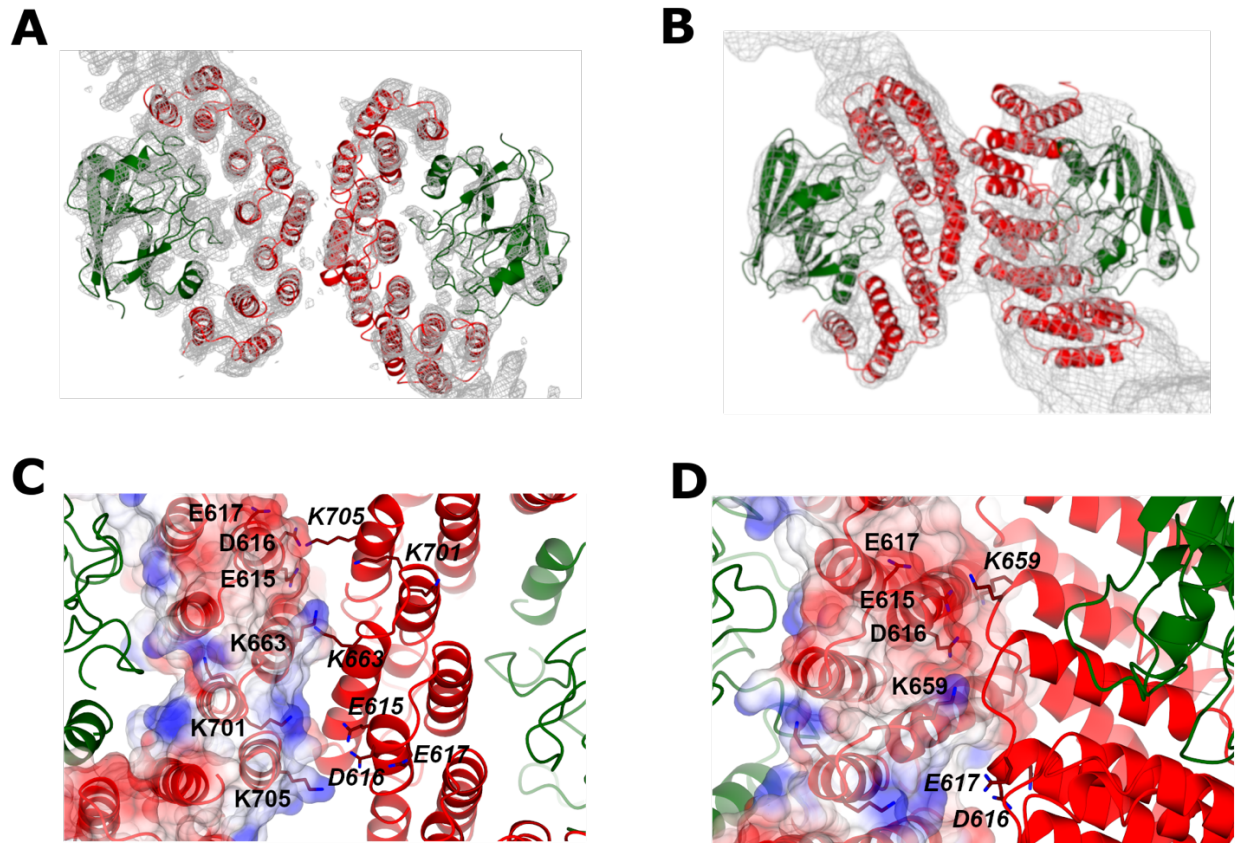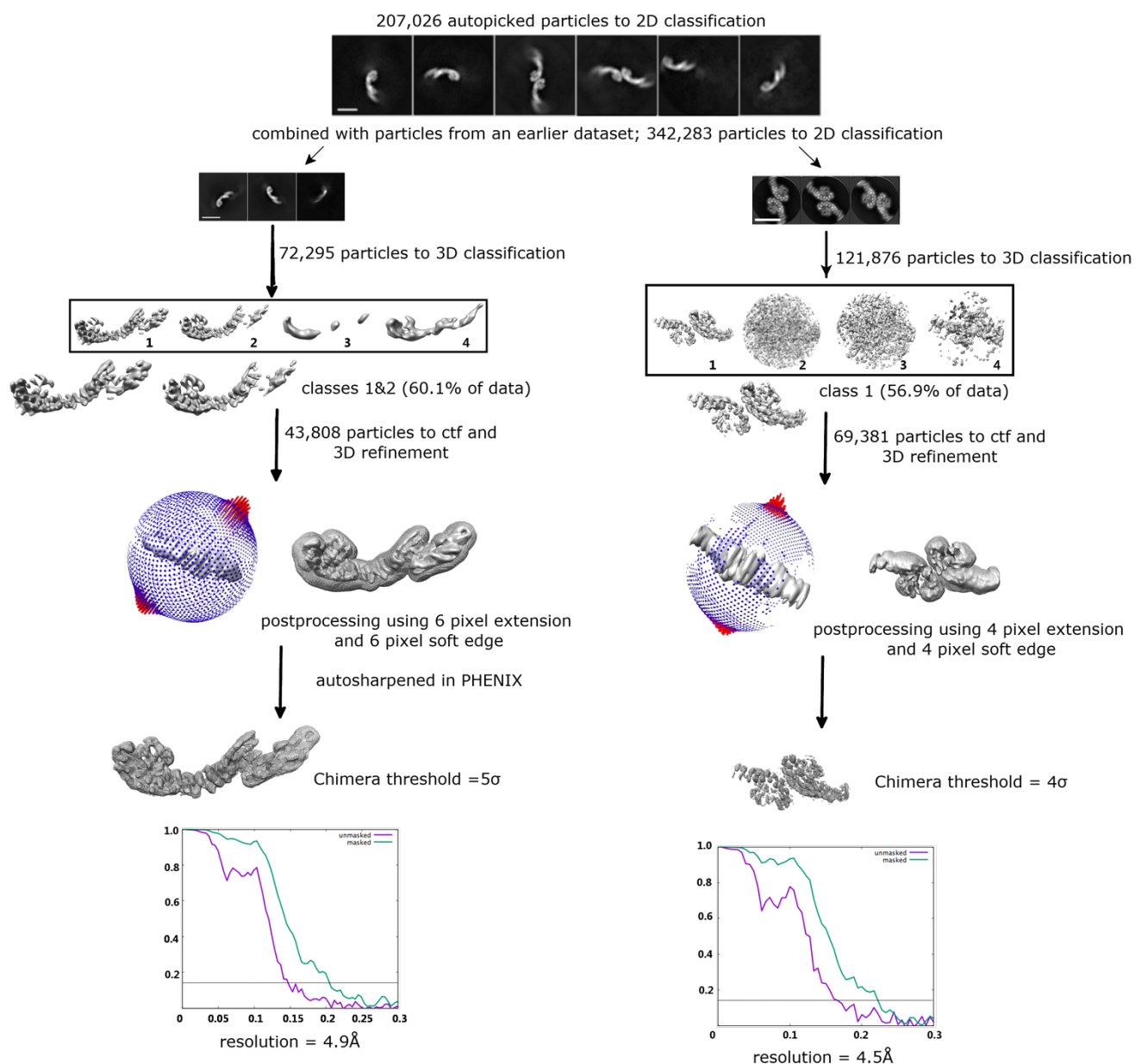
Figure 3. VPS35/VPS35 sub-structure reconstructions. (A) VPS35/VPS35 sub-structure interface determined from retromer chains is shown with fitted model. (B) VPS35/VPS35 sub-structure interface determined from retromer dimers of trimers (Figure 2) is shown with fitted model. Coulomb potential maps generated using CCP4MG are shown at 4σ (A) and 3σ (B) contour levels, respectively. (C, D) Close-up views of VPS35/VPS35 dimer interfaces observed in flat chains (C) and dimers of trimers (D). Improvements in data processing resulted in reconstructions with higher resolution; these structures further support the presence of specific electrostatic residues (E615, D616, E617, K663, K701, K705) mediating VPS35 dimer formation in asymmetric interfaces. Residues in the first dimer copy are labeled in black text, and residues in the second copy are labeled in black italic text.

Figure 4. Single particle reconstruction of the retromer 3KE mutant reveals a new interface. (A, B) Reconstructions of retromer 3KE particle (A) and its sub-structure (B) centered on the "chain link" mediated by VPS26 and VPS35. Coulomb potential maps generated using CCP4MG are shown at 5σ (A) and 3σ (B) contour level. (C, D) Local resolution of 3KE mutant (C) and sub-structure. (E, F) Angular distribution of 3KE mutant (E) and sub-structure (F). (G, H) Close-up views of the newly observed VPS26/VPS35 interface, in which the N-terminal VPS26 arrestin saddle interacts with the N-terminus of a neighboring VPS35 subunit.

A

B

Region	Symbol	Surface Area (Å²)
N-VPS35 (I) – C-VPS26 (I)		6987
N-VPS35 (II) – N-VPS26 (I)		7002
N-VPS35 (II) – C-VPS26 (II)		6382
N-VPS35 (I) – N-VPS26 (II)		6973

Figure 5. Analysis of retromer 3KE particle interfaces. (A) Schematic view of interactions observed in the retromer 3KE mutant particle. One heterotrimer is shown in dark colors (VPS29 in green, VPS35 in red, VPS26 in blue) and the second is shown in transparent colors. Within each heterotrimer, N-VPS35 binds C-VPS26A (black & grey hatched circles). Each "chain link" structure is held together by an interaction between a VPS35 N-terminus and the VPS26A N-terminal arrestin saddle in the neighboring heterotrimer (marked as black & grey circles). This interaction occurs on the opposite side from where the VPS35 N-terminus interacts with a VPS26A subunit within its own heterotrimer. (B) Summary of buried surface area analysis between VPS35 and VPS26A (calculated using PISA, full details in text).

Figure S1. CryoEM image and data processing work flow for updated retromer heterotrimer and VPS35/VPS35 sub-structure. Particles were auto-picked from three combined datasets using a 3D starting model (details in Methods). Particles were separated into 2D classes based on biochemical species (heterotrimer, flat chains). The left branch shows data processing pipeline for heterotrimers, and the right branch shows processing for the VPS35/VPS35 sub-structure reconstructed from flat chains. 3D reconstructions were generated for each species. Fourier Shell Correlation (FSC) plots showing masked and unmasked resolution estimates from RELION are shown for each structure or sub-structure; the grey line marks the 0.143 cut-off.
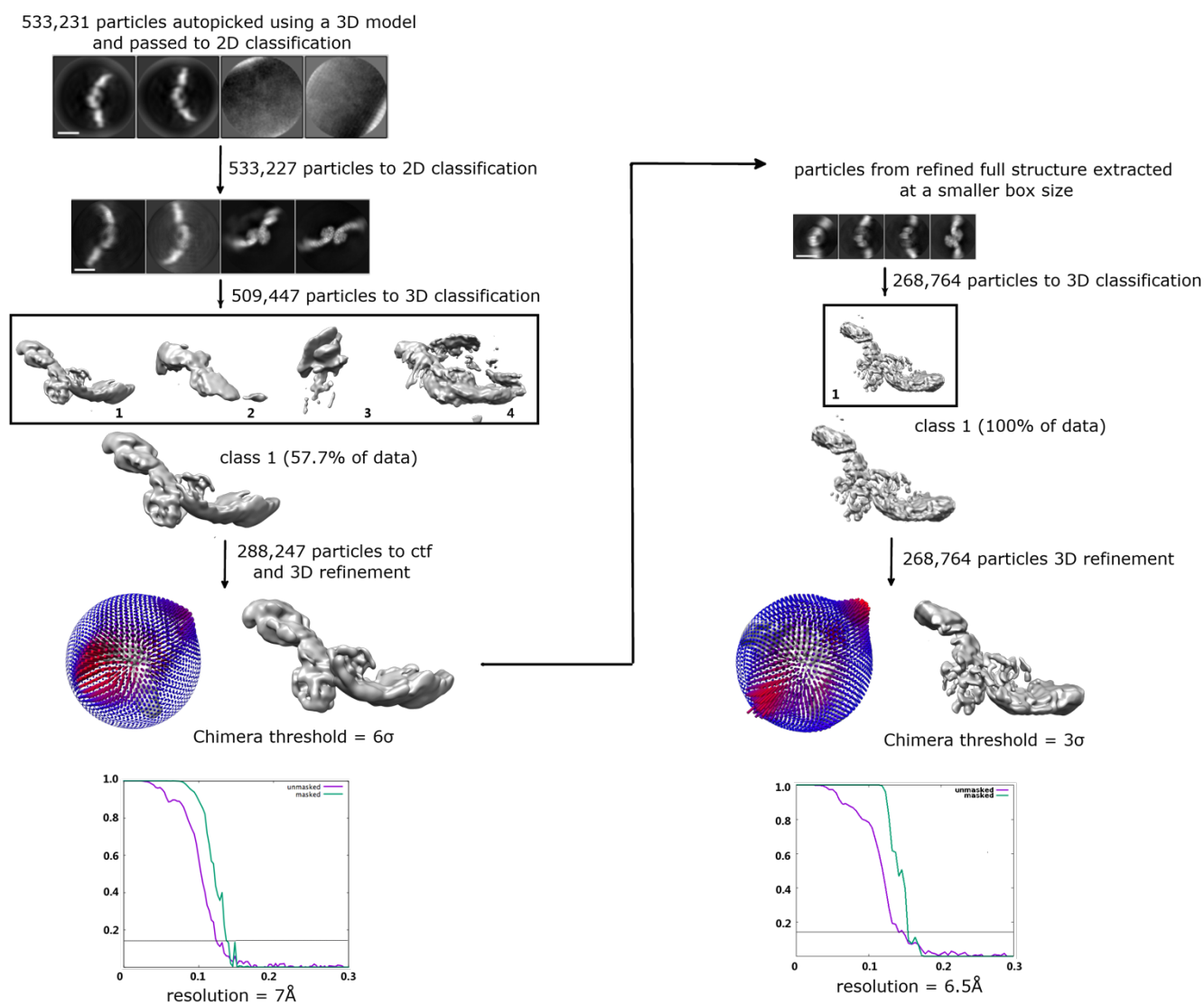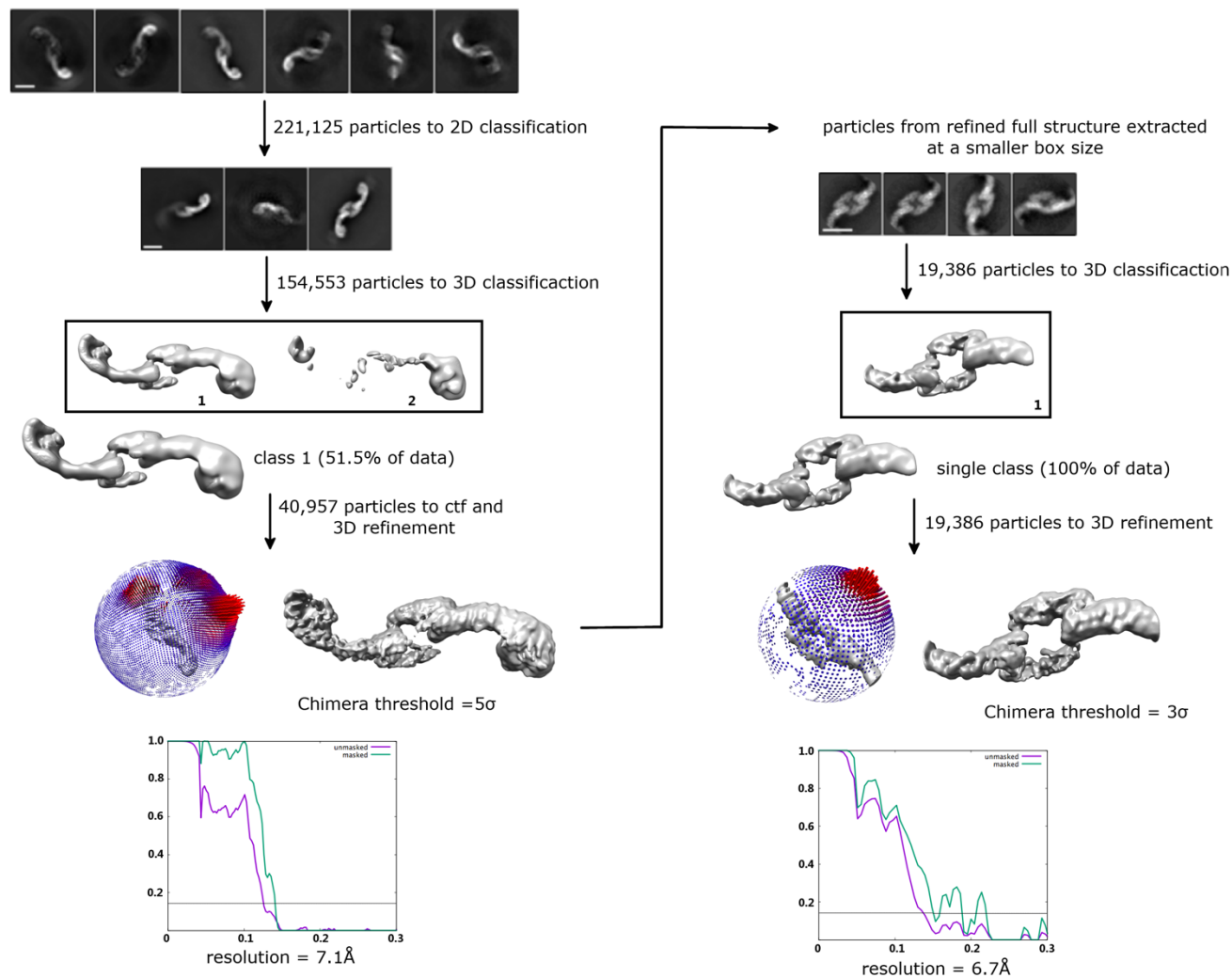
Figure S2. CryoEM image and data processing work flow for retromer dimers and sub-structure. Particles were auto-picked from a published dataset (Kendall, *Structure* 2020) using a 3D starting model of the retromer heterotrimer (details in Methods). Dimer particles were separated from other species during 2D classification, and 3D reconstructions were generated for both the intact dimer (left branch) and the VPS35/VPS35 sub-structure (right branch). Fourier Shell Correlation (FSC) plots showing masked and unmasked resolution estimates from RELION are shown for each structure or sub-structure; the grey line marks the 0.143 cut-off.
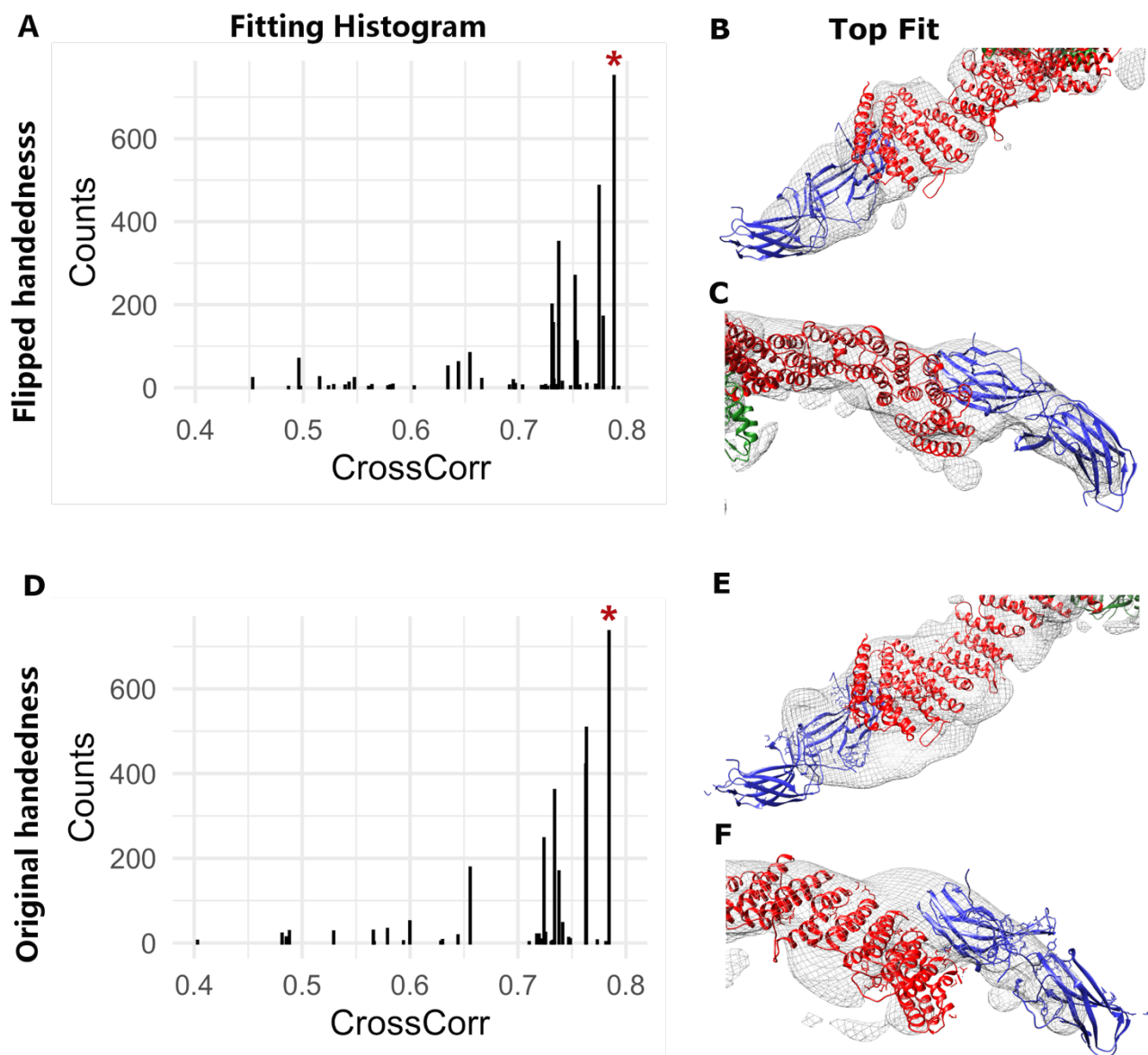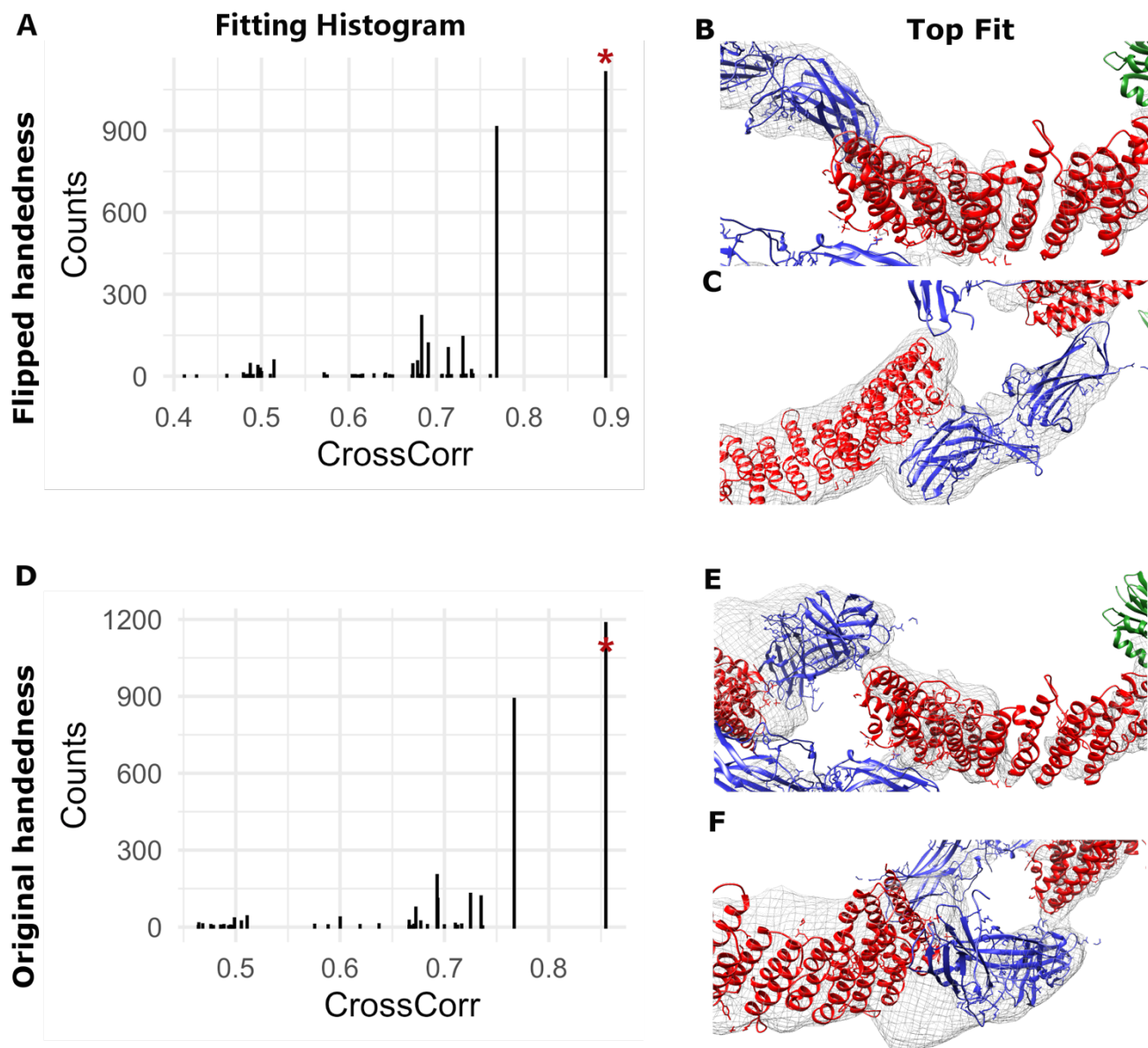
Figure S3. Analysis of retromer dimer map handedness. Map handedness was systematically analyzed by performing random rigid-body fits of real-space refined retromer models into each map (details in Methods). (A) Fitting histogram for flipped map handedness map showing counts of random rigid-body fits and cross-correlation values (Chimera). Magenta star marks top fit. (B,C) View of top fitted model in Coulomb potential map. Maps were generated using CCP4MG and are shown at 6σ contour level; VPS35 in red ribbons; VPS26 in blue ribbons; VPS29 in green ribbons. (D) Fitting histogram for original map handedness showing counts of random rigid-body fits and cross-correlation values (Chimera). (E, F) View of top fitted model in Coulomb potential map. Maps were generated using CCP4MG and are shown at 6σ contour level. This analysis suggests the flipped handedness (C, D) represents the correct handedness.

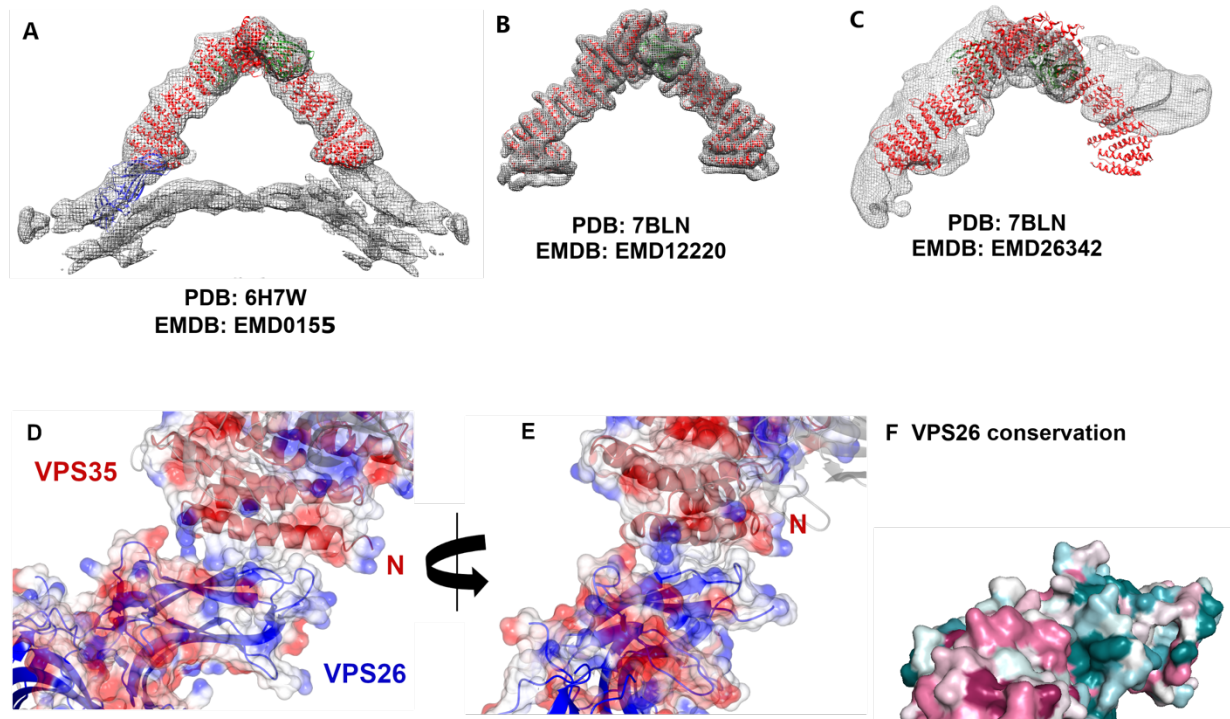275,663 particles autopicked using 3D model and passed to 2D classification

221,125 particles to 2D classification

particles from refined full structure extracted at a smaller box size

154,553 particles to 3D classificaction

19,386 particles to 3D classificaction

1   2

1

class 1 (51.5% of data)

single class (100% of data)

40,957 particles to ctf and 3D refinement

19,386 particles to 3D refinement

Chimera threshold =5σ

Chimera threshold = 3σ

resolution = 7.1Å

resolution = 6.7Å

Figure S4. CryoEM image and data processing work flow for retromer 3KE mutant. Particles were auto-picked from a single dataset using a 3D starting model (details in Methods). 3KE mutant particles were separated from other biochemical species during 2D classification, and 3D reconstructions were generated for both the intact dimer (left branch) and the sub-structure focusing on the chain link (right branch). Fourier Shell Correlation (FSC) plots showing masked and unmasked resolution estimates from RELION are shown for each structure or sub-structure; the grey line marks the 0.143 cut-off.

Figure S5. Analysis of retromer 3KE mutant map handedness. Map handedness was systematically analyzed by performing random rigid-body fits of real-space refined retromer models into each map (details in Methods); cross correlation coefficients and number of hits for each fit are shown. (A) Fitting histogram for flipped map handedness map showing counts of random rigid-body fits and cross-correlation values (Chimera). Magenta star marks top fit. (B, C) View of top fitted model in Coulomb potential map. Maps were generated using CCP4MG and are shown at 6σ contour level; VPS35 in red ribbons; VPS26 in blue ribbons; VPS29 in green ribbons. (D) Fitting histogram for original map handedness showing counts of random rigid-body fits and cross-correlation values (Chimera). (E, F) View of top fitted model in Coulomb potential map. Maps were generated using CCP4MG and are shown at 6σ contour level. This analysis suggests the flipped handedness (C, D) represents the correct handedness.

Figure S6. Analysis of retromer interfaces. (A, B) Equivalent views of published retromer arches are shown with their respective Coulomb potential maps from EMDB. (C) While individual retromer heterotrimers can be fitted as rigid bodies into the dimer map (cf. Figure 2; Figure S2), assembled arches are very poorly fitted as a single rigid body into the dimer map (rigid body fits in Chimera; full details in Discussion). (D, E) Two views rotated by 45 degrees of the N-VPS26A/N-VPS35 interface observed between a N-VPS35 (red ribbons) and N-VPS26A (blue ribbons) in a neighboring molecule; transparent electrostatic surface views are overlaid to demonstrate surfaces. The first helix of VPS35 (residues 12-36; labelled "N") interacts primarily with two β-strands (residues 48-56; 105-111) and two loops (residues 56-63; 101-105) in N-VPS26A. The overall shape of each subunit is complementary to its binding partner. (F) VPS26 conservation (ConSurf) mapped onto the VPS26A structure. The N-terminal interface with VPS35 does not exhibit high conservation levels across eukaryotes, suggesting this interface may not occur in all organisms with retromer.